

UCLA

UCLA Previously Published Works

Title

Controllable synthesis of layered black bismuth oxidechloride nanosheets and their applications in internal tumor ablation

Permalink

<https://escholarship.org/uc/item/5kx5b93c>

Authors

Fang, Qianlan
Xu, Yu
Luo, Lijia
et al.

Publication Date


2022-04-08

DOI

10.1093/rb/rbac036

Peer reviewed

Controllable synthesis of layered black bismuth oxidechloride nanosheets and their applications in internal tumor ablation

Qianlan Fang^{1,2}, Yu Xu^{1,2}, Lijia Luo^{1,2}, Chuang Liu^{1,2}, Zihou Li^{1,2}, Jie Lin^{1,3}, Tianxiang Chen^{1,3,*}, and Aiguo Wu ^{1,3,*}

¹Cixi Institute of Biomedical Engineering, International Cooperation Base of Biomedical Materials Technology and Application, Chinese Academy of Science (CAS) Key Laboratory of Magnetic Materials and Devices and Zhejiang Engineering Research Center for Biomedical Materials, Ningbo Institute of Materials Technology and Engineering, CAS, Ningbo 315201, P.R. China;

²University of Chinese Academy of Sciences, Beijing 100049, P.R. China;

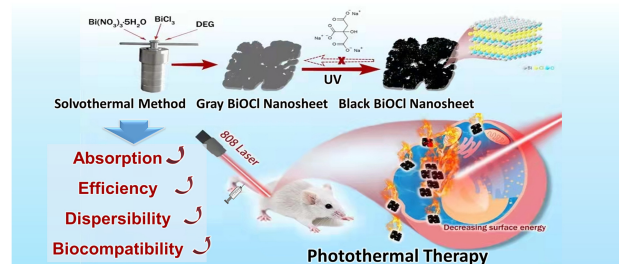
³Advanced Energy Science and Technology Guangdong Laboratory, Huizhou 516000, P.R. China

*Correspondence address. E-mail: chentx@nimte.ac.cn (T.C.); aiguo@nimte.ac.cn (A.W.)

Abstract

The recently emerging bismuth oxyhalide (BiOX) nanomaterials are promising indirect band gap photosensitizer for ultraviolet (UV) light-triggered phototherapy due to their unique layered nanosheet structure. However, the low absorption and poor photothermal conversion efficiency have always impeded their further applications in cancer clinical therapy. Herein, BiOCl rich in oxygen vacancies has been reported to have full-spectrum absorption properties, making it possible to achieve photothermal property under near-infrared laser. Under 808 nm irradiation, the photothermal conversion efficiency of black BiOCl nanosheets (BBNs) is up to 40%. BBNs@PEG can effectively clear primary subcutaneous tumors and prevent recurrence, achieving good synergistic treatment effect. These results not only broke the limitation of UV on the BiOCl material and provided a good template for other semiconductor materials, but also represent a promising approach to fabricate BBN@PEG a novel, potent and multifunctional theranostic platform for precise photothermal therapy and prognostic evaluation.

Keywords: black bismuth oxidechloride nanosheet; photothermal therapy; tumor; photothermal conversion efficiency



Introduction

Near-infrared-light-(NIR, 700–1100 nm) mediated photothermal therapy (PTT) refers to the method that under the excitation of a certain wavelength light, photothermal conversion reagents absorb photons and release heat, thereby increasing the local temperature of the tumor, changing the environment of the tumor cells and making them degenerate, to achieve the purpose of treating the tumor [1, 2].

As a new type of tumor therapy similar to photodynamic therapy, PTT has attracted much more attention for its advantages of non-invasive, short treatment time, simple operation and remarkable curative effect [3, 4]. In addition, it can also be used as a **supplementary therapy** for cancer treatment such as chemotherapy and radiotherapy, which can improve the therapeutic effect by 50% [5, 6]. Photosensitizers play a decisive role in PTT and have become the focus of researchers all over the world.

The most widely studied photosensitizers are mainly divided into organic and inorganic photosensitizer [7–10]. Organic photosensitizer mainly refers to some NIR organic dyes

[indocyanine green (ICG), IR825, etc.] and polymer nanomaterials (polyaniline, polypyrrole, dopamine, etc.) [8, 10]. The organic photosensitizer has good biocompatibility, but there are some obvious problems in their applications, such as low NIR absorption, relatively low photothermal conversion efficiency, easy photobleaching and poor material properties [11]. Inorganic materials are mainly composed of noble metal nanomaterials (gold nanorods, nanoshells, palladium, nanoparticles) [1, 2, 12–17], carbon nanomaterials (graphene oxide, carbon nanotubes, carbon quantum dots) [18–24], transition metal sulfides (copper sulfide, molybdenum sulfide, tungsten sulfide) [25–28], Prussian blue nanoparticles and black phosphate nanomaterials [29] and metallic oxide (bismuth oxide, titanium oxide) [30–33]. Compared with organic photosensitizer, inorganic photosensitizer has attracted more and more attention in the field of biomedicine due to their simple and controllable synthesis, high absorptivity, high photothermal conversion efficiency and good imaging function, and have broad application prospects in clinical trials later [7, 9, 34].

Received: December 18, 2021. Revised: March 13, 2022. Accepted: March 22, 2022

© The Author(s) 2022. Published by Oxford University Press.

This is an Open Access article distributed under the terms of the Creative Commons Attribution License (<https://creativecommons.org/licenses/by/4.0/>), which permits unrestricted reuse, distribution, and reproduction in any medium, provided the original work is properly cited.

In recent years, as a new anti-tumor photosensitizer, inorganic bismuth-based materials have been extensively studied in the diagnosis and treatment of cancer due to their unique physical and chemical properties, strong NIR absorption capacity and excellent photothermal conversion performance [14, 35–40]. In addition, these materials have the advantages of simple synthesis method, low cost, long circulation time *in vivo* and good dispersion. Although Bismuth-based nanomaterials have been extensively studied in the field of catalysis, the research in biomedicine is still in its infancy. Although nanomaterials such as Bi_2Se_3 and Bi_2S_3 can obtain good photothermal effects in mouse tumor models, the cytotoxicity, instability and the poor photothermal conversion efficiency bismuth-based nanoparticles have been the main problems limiting their application in biomedical field.

BiOCl was originally one of the excellent materials in photocatalytic applications; there were a number of researchers using solvothermal reaction, photochemical reaction and high-temperature calcination reduction method, which endowed abundant BiOCl material defects, widening its absorption spectrum, from originally ultraviolet (UV) excitation to photocatalytic reaction under the visible light. OVs are the most prevalent and widely studied anion defects with a relatively lower formation energy on oxide surfaces. The OV-induced localized states could extend light response to visible/IR light and efficiently trap charge carriers, giving rise to the enhanced photoreactivity [38].

Our group first reported on the application of BiOCl -based nanomaterials in biomedicine [41]. The BiOCl nanoplates and BiOCl nanosheets (BBNs; $200 \mu\text{g ml}^{-1}$) achieved high PDT efficacies (about 90% tumor cell killing) under UV irradiation (low UV power density 2.2 mW cm^{-2} , 30 min). Despite its high capability, the white BBN still got its shortage, such as the cytotoxicity, the instability and most important, the phototoxicity of UV light. Cheng *et al.* used the defect of BiOCl for tumor phototherapy, but a photothermal conversion efficiency of black BBNs was 13.9% in previous reported work, which was more lower than other inorganic nanomaterials for example gold nanoparticles [42]. It urgently to develop new synthesis of BBNs with high photothermal conversion efficiency for their biomedical applications.

In this study, we developed a solvothermal synthesis method for black BBN with sodium citrate modified and exposure to UV light (Fig. 1). We have found that the black BBN is not only with an excellent stability and inoxidizability but also an ideal photosensitizer with wider range of absorption, high conversion efficiency (up to 40%) and great biocompatibility. The improvement on the application of black BBN is critical in PTT of tumor, besides filling in gaps in photothermal application of wide-band gap semiconductor.

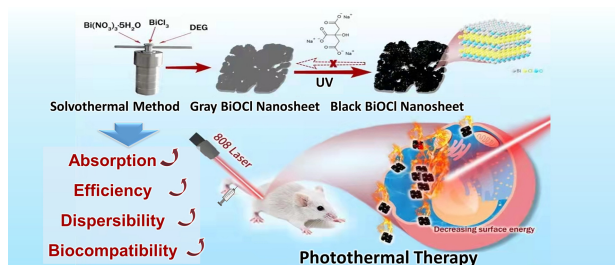


Figure 1. Schematic illustration of synchronized photothermal effect of BiOCl NSs with OV contents NIR (808 nm) irradiation.

Materials and methods

Materials

The reagents used in this work have been listed in Table 1 and the instruments used in this work have been listed in Table 2 as following.

Synthesis of black BiOCl intermediate

Black BiOCl intermediate was synthesized according to previously reported method with slight change. Briefly, 2 mmol (970 mg) $\text{Bi}(\text{NO}_3)_3 \cdot 5\text{H}_2\text{O}$ was dissolved in 40 ml diethylene glycol in a 50-ml glass vial. When it was completely dissolved after ultrasonic treatment, 1 mmol (315.5 mg) BiCl_3 was added in the vial. After ultrasonic treatment to transparent, the solution was transferred to 50 ml hydrothermal reactor, which was heated for 12 h under the temperature of 180°C degrees for hydrothermal reaction and then natural cooled down to room temperature naturally, the sediment was washed several times with water and ethanol and dried at 80°C for 10 h, $\text{BiO}_0.7\text{Cl}$ NSs was collected for the following experiment.

Synthesis of black BBNs

Five milligrams intermediate mentioned above was dissolved into 10 ml aqueous solution of trisodium citrate with the concentration of 50 mg ml^{-1} (and now the concentration of intermediate is $500 \mu\text{g ml}^{-1}$). Then, the solution was separated to glass tubes and treated with the photochemical reaction instrument for 2 h, the UV light was provided by 500 W mercury lamp with UV filter. After that, the product was cleaned with water and ethanol for several times and collected by centrifugation and dried in oven at the temperature of 60°C .

BBN@PEG: 5 mg of BBN and 500 mg of PEG were added in 10 ml ethanol under magnetic stirring at ambient condition. The mixture was allowed to be incubated overnight for the PEG to decorate of the BBN. After that, the sediment was cleaned with water and ethanol for several times. When the reaction finished, sediment was gathered and purified by centrifugation at 10 000 rpm for 10 min with DI water and ethanol washing for several times. Then, synthesized BBN@PEG was re-dispersed in DI water.

Table 1. Reagents used in this work

Reagent	Purity	Source
Sodium citrate Tribasic dehydrate	99%	SIGMA
DEG	99%	Aladdin
BiCl_3	AR	Aladdin
Chloral hydrate	AR	Aladdin
$\text{Bi}(\text{NO}_3)_3 \cdot 5\text{H}_2\text{O}$	99%	Aladdin
Mannitol	99%	Aladdin
Milli-Q water		
NaCl	99.5	J&K
Ethanol absolute	AR	Sinopharm
PVP		Sinopharm
PEI	99%	Aladdin
FBS		Gibco
RPMI-1640		Gibco
MTT		
PBS		
KCl	AR	Sinopharm
Na_2HPO_4	99%	Aladdin
KH_2PO_4	AR	Sinopharm
DMSO	>99.8%	Aladdin
BSA		Gibco
Trypsin-EDTA		Gibco

Table 2. Instruments used in this work

Instruments	Model
NIR Laser Device	DS2-11312-403
Thermal Imager	JM500XC
Electronic Scales	ME104/02
Ultrasonic Cleaners	SB25-12DTDN
Magnetic Stirrers	HJ-6
Draught Drying Cabinet	DHG-9145A
Centrifuge	TGL-15B
Ultracentrifuge	ST 16R
Ultrasonic Processor	XC-CD
Carbon Dioxide Incubator	1501
Thermostat Water Bath	HH-6
Autoclave Sterilizer	MLS-3750
Refrigerator	BCD-226ST V
ELIASA	iMarkTM
Microscope	NIB-100
Fluorescent Microscope	3000B
Biosafety Cabinet	KS18
Ultra-low Tem Freezer	Forma 700
Low Speed Centrifuge	TDL-40C
TEM	JEM-2100F
ICP-OES	Spectro Arcosii
ZETA	Zetasizer Nano ZS
UV-Vis	T10CS
Photochemical Reactions	XPA

Synthesis BBN@PEG

One gram of PEG was completely dissolved in 20 ml absolute ethyl alcohol after 20 min ultrasonic processing. Then, 5 mg of as-prepared BBNs was dispersed in the solution. After stirring for 24 h, the product was cleaned with water and ethanol for several times and collected by centrifugation and resuspended in 10 ml of deionized water.

Photothermal conversion experiment of BBN

Photothermal conversion efficiency was calculated by temperature elevation under the 808 nm laser irradiation. The above prepared BBN was dispersed into ultra-pure water with concentrations of 100, 200, 300, 400 and 500 $\mu\text{g ml}^{-1}$ obtained through dilution. Take 1 ml solution of each concentration to transfer to the cuvette, using the wavelength of 808 nm infrared diode laser irradiation (this experiment using optical power density of 1 W cm^{-2}) for 5 min. At the same time, adjust the light spot size to make it just cover liquid section and use the thermal imager real-time access to the temperature change of the sample solution during illumination. At the end of the experiment, the temperature and time curves of samples with different concentrations were obtained to calculate the photothermal conversion efficiency.

Cell line and cell incubation

Murine breast cancer cell line 4T1 was cultured in RPMI 1640 medium (Gibco) supplemented with 1% penicillin/streptomycin and 10% heat-inactivated fetal bovine serum (FBS) in a 5% CO_2 incubator at 37°C.

In vitro cytotoxicity of BBN@PEG

One hundred microliters of 4T1 cells suspension was seeded into the 96-well plate per well at cell density about 1×10^4 cells per well. *In vitro* cytotoxicity of BBN@PEG was determined by MTT assay. After overnight incubation, all the original medium were removed, and RPMI containing BBN@PEG nanosheet samples with different concentrations (0, 100, 200, 300, 400, and 500 $\mu\text{g ml}^{-1}$) was added to each well, and after another incubation for 24 h. Subsequently, 10 μl of MTT (5 mg ml^{-1} in PBS) the above MTT

solution was added to each well of the 96-well plate. After 4 h incubation, all the liquid in the 96-well plate was removed and 100 μl of DMSO solvent was added to each well to dissolve the formazan crystals formed in cells. Finally, the absorbance was measured by a microplate reader at the wavelength of 550 nm, which is the characteristic absorption peak of formazan, to determine the relative number of remaining living cells in each well.

In vitro PTT of BBN@PEG

The 4T1 cells were seeded in the 96-well plate with a density of 1×10^4 cells per well for 24 h to make the cells stick to the wall. Then, all the original medium in the 96-well plate were removed, and RPMI-1640 containing BBN@PEG with different concentrations (0, 100, 200, 300, 400 and 500 $\mu\text{g ml}^{-1}$) was added to the corresponding wells according to the design and incubated for another 4 h. Each well was then washed with PBS and 100 μl fresh RPMI-1640 was added to each well. Then the cell plates of the photothermal treatment group were placed under 808 nm laser for laser irradiation. Experimental variables (laser power density and laser exposure time) were controlled. After the photo treatment, the cells were incubated for another 24 h. Then, 10 μl of the MTT solution dispersed in PBS at a concentration of 5 mg ml^{-1} was added to each well of the 96-well plate. Four hours later, all the liquid in the 96-well plate was removed and 100 μl of DMSO solvent was added to each hole to dissolve the formazan crystals formed in cells. Finally, using the microplate reader reads absorbance of each well at 550 nm, to determine the relative number of remaining living cells in each hole.

Living-death cell staining experiment

Calcein-AM/PI double stain kit from Yeasen was used for live/dead cell staining. In a typical experiment, 4T1 cells were seeded in the 96-well plate with a density of 1×10^4 cells per well for 24 h to make the cells stick to the wall. Then, all the original medium in the 96-well plate was replaced for RPMI containing BBN@PEG nanosheets with different concentrations (0, 100 and 500 $\mu\text{g ml}^{-1}$) and incubated for another 4 h. Thereafter, the cells in each well were irradiated by 808 nm for another 5 min. After laser irradiation, the cells were cultured for another 24 h and stained by Calcein-AM/PI working solution for 15 min at 37°C. The fluorescence of cells was evaluated by fluorescent microscope.

Animal models

Briefly, female BALB/c nude mice with body weight of 18–22 g aged 6 weeks were injected subcutaneously with 100 μl (1×10^6) cells in RPMI were on the right flank of back, and all animal experiments followed were performed when the tumor reached about 100–150 mm^3 [Tumor volume (V) = length \times width²/2]. All procedures used in this experiment were compliant with the local animal ethics committee.

In vivo PTT of BBN@PEG

Tumor models were established on 5-week-old Balb/C females mice. Tumor size was measured with digital calipers. Tumor volume = tumor length \times (tumor width²)/2. When the tumor diameter reached 3–4 mm, the mice were randomly divided into four groups, each group containing 6 mice. Mice were anesthetized by intraperitoneal injection of chloral hydrate solution with a mass fraction of 8%, and then intravenous (i.v.) injection of 50 μl sample aqueous solution (at a concentration of 2 mg ml^{-1}) or 50 μl normal saline. The tumor site was exposed or not exposed to 808 nm laser (power density = 1 W cm^{-2}) for 5 min. After the

illumination, tumor size was measured by digital caliper for 14 days, and then the tumor volume was calculated by formula.

Results and discussion

Preparation and characterization of B-BiOCl nanomaterials

As evidenced by the transmission electron microscopy (TEM) images (Fig. 2a), the BBNs had a uniform size (~ 150 nm) with obvious surface defect. Then, we performed the high-angle annular dark-field scanning TEM (HAADF-STEM)-based elemental mapping (Fig. 2a) as well as energy-dispersive X-ray mapping, the images have further confirmed the structure and uniform distribution of element, which indicated BBNs crystal growth with high uniformity. High-resolution TEM (HR-TEM) image showed the lattice structure of BBNs with a lattice spacing of 0.734 nm (001) corresponding to the (001) crystal plane spacing of BBN, and 0.276 nm matched with the (110) crystal plane spacing (Fig. 2b). The X-ray powder diffraction (XRD) pattern showed the standard spectrum of the crystal BBN, which matched with the typical lattice planes (Fig. 2c). The peaks at 4f7 and 4f5 in X-ray photoelectron spectroscopy (XPS) are the characteristic peaks of bismuth element in BBN crystal (Fig. 2d), which further confirmed the successful fabrication of BBNs. In addition, the introduction of oxygen vacancy was further confirmed from the UV-vis-NIR absorbance spectra (Fig. 2e). Before the reduction reaction, the precursor of BBNs can only absorb UV light, and it is crucial to improve the bismuth-based.

The photothermal conversion experiment of BBN

Photothermal conversion efficiency is an important criterion for evaluating the quality of photothermal conversion reagents.

Encouraged by the high absorption in NIR region, the photothermal conversion properties of the materials were tested. The experimental results (Fig. 3a) showed that the aqueous solution of black BBNs heated rapidly under NIR excitation at 808 nm, with a concentration of $100\text{--}500\ \mu\text{g ml}^{-1}$, when the laser power density was set to $1\ \text{W cm}^{-2}$. The extinction coefficients of BBN@PEGs were determined to be $10.08\ \text{l g}^{-1}\ \text{cm}^{-1}$ (Fig. 3d and e), indicating BBN@PEG's high ability of photothermal conversion efficiency. The photothermal properties of BBN@PEG aqueous solution upon an 808 nm laser irradiation *in vitro* were systematically studied at different concentration under laser power density of $1\ \text{W cm}^{-2}$ (Fig. 3d), evaluated by a digital NIR photothermal imaging system. The deionized water showed little change under laser irradiation; however, BBN@PEG presented a sharp contrast of temperature increasing to 70°C in 10 min. These results imply that the BBN@PEG has a stable ability to convert NIR energy to thermal energy rapidly and efficiently. Moreover, the photothermal conversion efficiency has been calculated to be $\sim 40\%$ according to the reported methods (Fig. 3e). Then, the study on photostability of BBN@PEG was also clearly investigated that upon the continuous irradiation by NIR laser for 1 h. Under the laser illumination, BBN@PEG has no obvious impairment, indicating good photostability, which is very important toward further practical applications. Therefore, the excellent photothermal conversion efficiency and photostability of BBN@PEG make it to be a promising PTT agent with a remarkable potential.

Biotoxicity test and PTT effect studying of BBN@PEG *in vitro*

Next, the cytotoxicity of these BBN@PEG is also a necessary part to study or further biomedical applications as well. The 4T1 cells

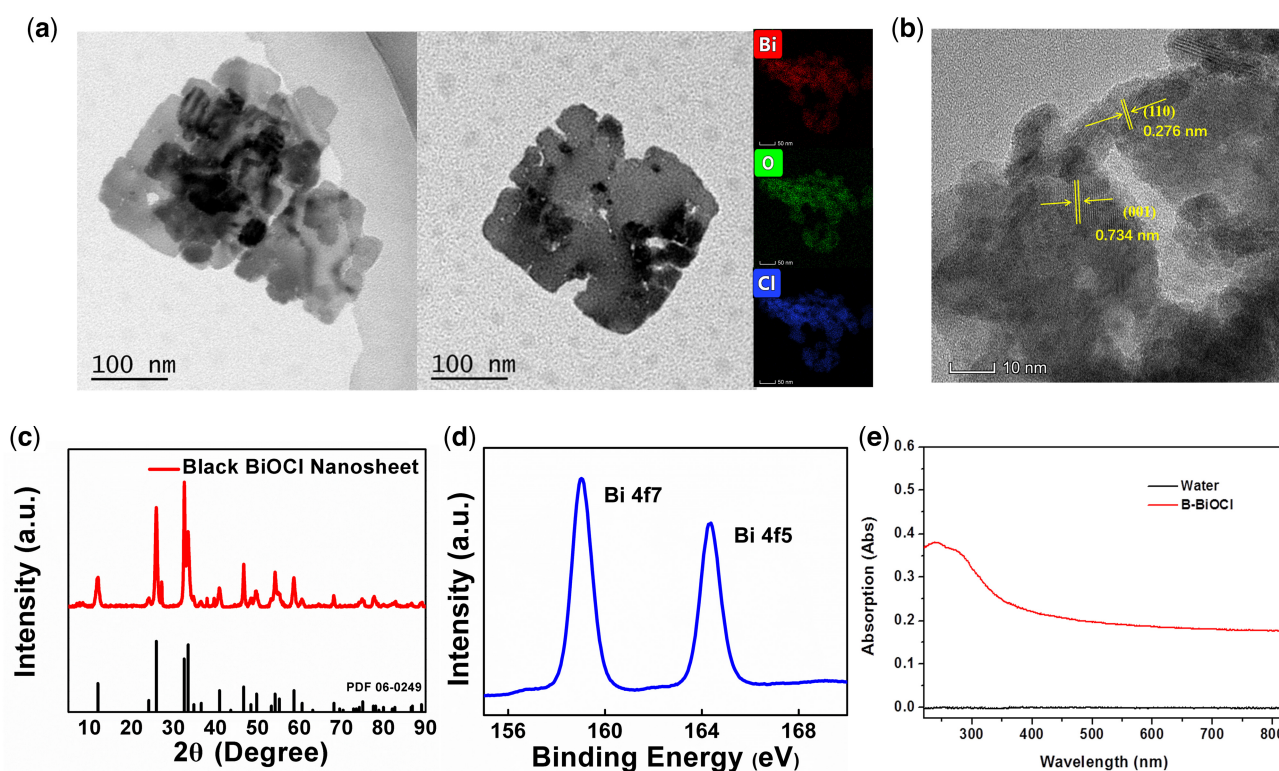


Figure 2. Synthesis and characteristic of BBNs. (a) TEM and EDS mapping of BiOCl. (b) HR-TEM images and of BBNs and crystal planes of 0.734 nm of (001), 0.276 nm of (110). (c) XRD patterns of BBNs. (d) XPS Bi 4f spectrum of BBNs. (e) UV-vis absorption spectra of BBNs.

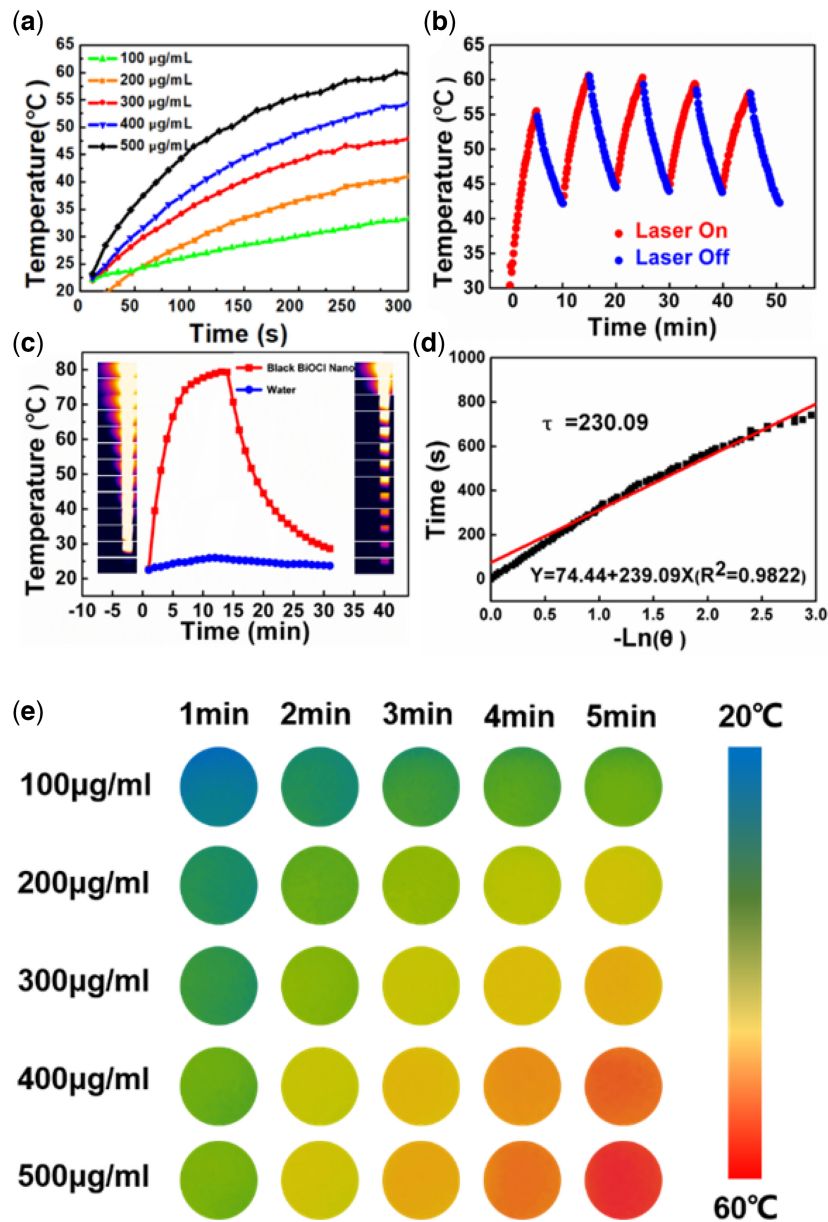


Figure 3. Photothermal effect and photothermal stability of BBNs. (a) Temperature elevation profiles of BBNs with 808 nm laser irradiation (1 W cm^{-2} , 5 min). (b) The photothermal profiles of BBNs aqueous dispersions ($200 \mu\text{g ml}^{-1}$) over five irradiation cycles. (c) The heating and cooling curves of BBNs (2 W cm^{-2}). (d) The fitting curve of the absorption values at 808 nm of BBNs dispersions at different concentrations in water. (e) NIR photothermal images of BBNs aqueous solution under different irradiation conditions for 5 min under 808 nm laser irradiation (1 W cm^{-2} , 5 min).

that were incubated with BBN@PEG for different concentration, the standard 3-(4,5-dimethyl-2-thiazolyl)-2,5-diphenyl-2h-tetrazolium bromide (MTT) assay (Fig. 4c and d) and live/dead staining (Fig. 4e) were performed, indicating that BBN@PEG has a good biocompatibility. For example, even at a concentration as high as of $500 \mu\text{g/ml}$, the cell viability of 4T1 cell remains more than 80% (Fig. 4c). Due to the high level of internalization property and nontoxicity, the *in vitro* PPT was carried on for forward verification of BBN@PEG therapeutic performance. The 4T1 cell was incubated with BBN@PEG for different concentration for 4 h, after washed off of BBN@PEG, the cells were exposed to 808 nm laser (power density = 1 W cm^{-2}) for 5 min. Cells only exposed to laser remain alive, on the other side, the viability of cells incubated with BBN@PEG upon the NIR laser exposure has dramatically decreased to only $\sim 20\%$ (Fig. 4d), meaning BBN@PEG

high photothermal property on killing cancer cells upon NIR irradiation.

Biotoxicity and test *in vitro*

In vivo cancer treatment experiment is an integral part for BBN@PEG to be nontoxic as well as biocompatible for organism. Blood routine examination (Fig. 5a–d) and blood biochemistry examination (Fig. 5e–h) were employed for nanomedicine safety monitoring. Healthy BALB/c mice were injected with BBN@PEG through caudal vein, and the blood sample was collected in next 6 h, 1, 3, 7 day for above-mentioned test. As showed in Fig. 5, the value of white blood cell (WBC), red blood cell (RBC), hemoglobin (HGB) and platelet (PLT) before and after injection almost unchanged, meanwhile, blood biochemistry examination is to test the levels of various ions, sugars, lipids, proteins, enzymes,

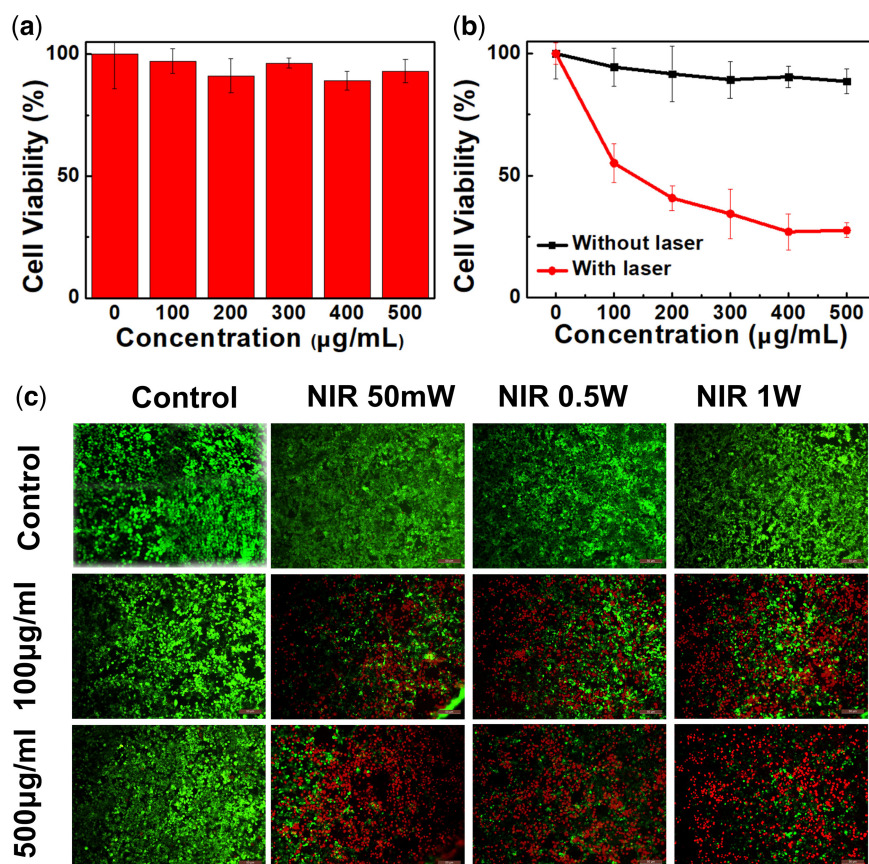


Figure 4. Biotoxicity test and PTT effect studying of BBN@PEG *in vitro*. (a) Cell viability assessments of 4T1 cells treated with BBN@PEG (0–500 $\mu\text{g mL}^{-1}$) for 24 h without laser irradiation or (b) with 808 nm laser irradiation for 5 min (1 W cm^{-2}). (c) Live/dead staining of 4T1 cells treated with BBN@PEG (100 and $500 \mu\text{g mL}^{-1}$) for 4 h with 808 nm laser irradiation for 5 min at 1 W cm^{-2} .

hormones and metabolites present in the blood are measured. The main four parameters were chosen to monitor hepatorenal function. The value of aspartate aminotransferase (AST), alanine aminotransferase (ALT), blood urea (UREA) and creatinine (CREA) changed obviously 1 day after injection, nevertheless gradually return to normal in next few days, which notify BBN@PEG safety in hematology. To further testify if BBN@PEG were toxic to main organs *in vivo*, H&E stain was performed before and after injection in 6 h, 1, 3, 7, and 14 days. Comparing control group with injection group, there's scarcely injury and inflammation was observed.

PTT effect studying of BBN@PEG *in vivo*

One of the best advantages of PTT is its much-limited damage to surrounding healthy tissue, controllable therapeutic process and avoiding the destruction induced by external laser radiation, which raise an essential precondition that the nanomedicine could gather to solid tumor based on the enhanced permeability and retention effect. Base on the above, the investigation of the BBN@PEG *in vivo* PTT was performed on 4T1 bearing mice model. To study the practicability BBN@PEG for oxygen-vacancy-enhanced PTT based on their outstanding performance of photothermal conversion, the 4T1 bearing mice were separated into following four groups until the tumor volume to $\sim 150 \text{ mm}^3$, which are (i) PBS injection alone (PBS), (ii) laser irradiation alone (Laser), (iii) BBN@PEG *i.v.* injection alone (BBN@PEG) as well as (iv) BBN@PEG *i.v.* injection with laser irradiation (BBN@PEG + Laser). Figure 6a obviously shows that 4T1-bearing mice injected with PBS scarcely show response to the laser irradiation, which made a great contradiction to mice injected with BBN@PEG whose

temperature raised from 30.9°C to 60.9°C in 300s exposed to 808 nm laser (power density = 1 W cm^{-2}). Next, 24 h after *i.v.* injection with or without laser irradiation (day 0), the tumor volumes (Fig. 6c) and the mice body weights (Fig. 6d) of mice were recorded every second day, which demonstrated the PBS, BBN@PEG and NIR laser irradiation all had neglectable effect on tumor growing. In BBN@PEG + Laser group, five in six mice had a full recovery without any evidence of recurrence. The relative survival rates (Fig. 6d) have been observed for 45 days, and there was still no death in BBN@PEG injection with laser irradiation group, further proving the distinct differences among all of the groups' therapeutic efficiency. Figure 6f manifest representative pictures were taken of mice on the 14th day. H&E staining (Fig. 6g) was employed to verify the impairment and inflammation response on cellular level, presenting a large area of extensive necrosis of tumor tissue and necrotic nidus was eosinophilic, showing pink. Moreover, there was karyopyknotic in nucleus of necrotic tumor cells, the staining is deepened meanwhile fragmented and lysed, accompanied by a small area of bleeding and calcification after necrosis was also visible. Taken all together, BBN@PEG can accumulate in tumor region efficiently, presenting potent photothermal therapeutic effect, on which based NIR light-triggered PTT could be a reliable and efficient cancer treatment strategy.

Conclusions

In summary, we synthesized a biocompatible, precise and multi-functional BBNs nanoplatform for PTT therapy of tumor, whose

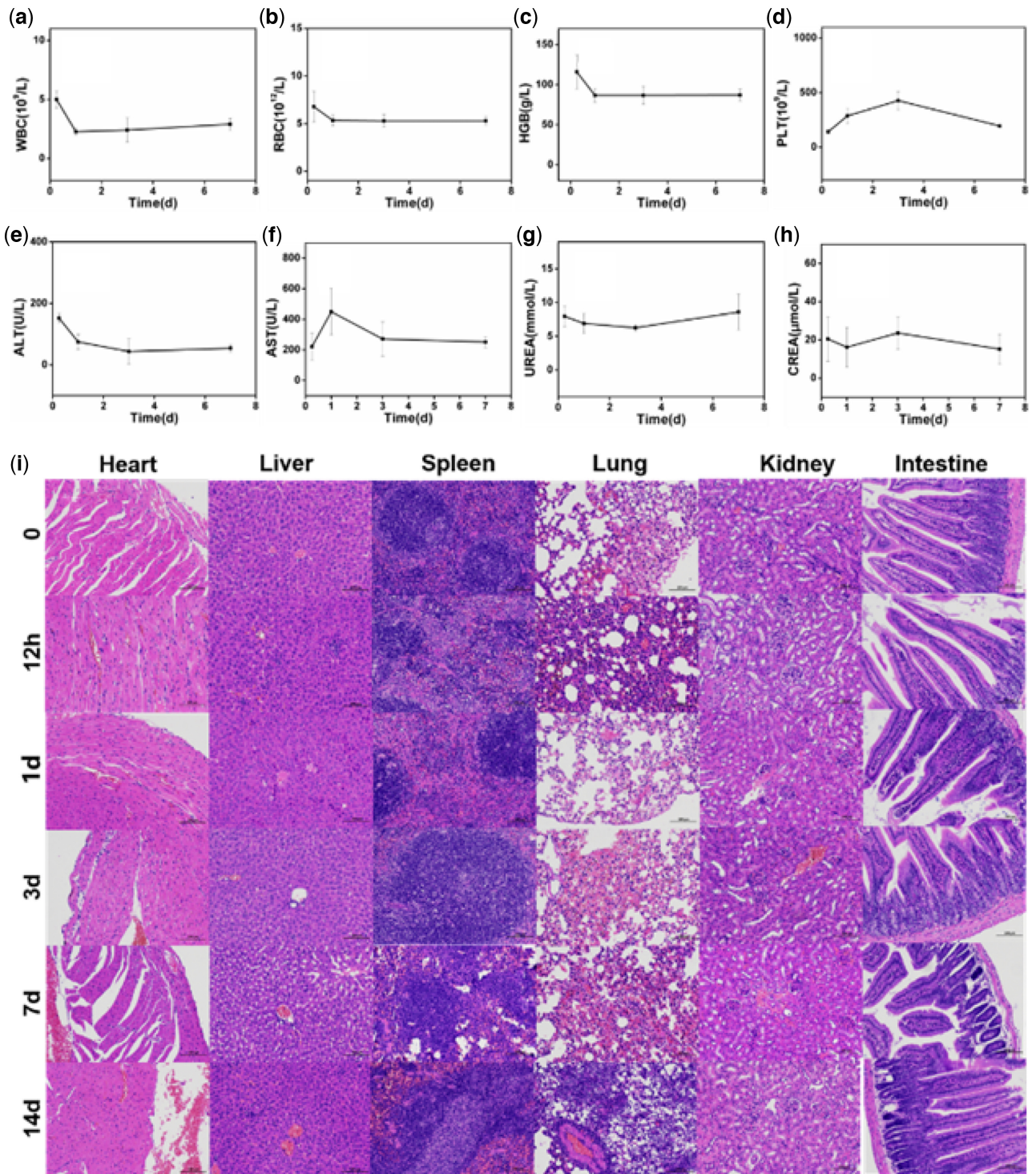


Figure 5. Hematological examination and pathological section of main organs of mice after i.v. injection of $50\ \mu\text{l}$ BBN@PEG ($2\ \text{mg}\ \text{ml}^{-1}$). (a–d) Blood routine examination of blood cell (WBC), RBC, HGB and PLT. (e–h) blood biochemistry examination of AST, ALT, UREA and CREA.

high photothermal conversion efficiency was enhanced by excellent oxygen vacancy defect structure. The as-prepared BBN@PEG process strong broad NIR absorbance, which is specifically devised for PTT and tumor ablation. The thermography for 4T1-bearing mice showed that tumor cell squint toward complete phagocytosis BBN@PEG, resulting in fantastic therapeutic effect for cancer cell. The results of 4T1 bearing mice with 100%

survival rate show that the BBN@PEG had excellent diagnostic and therapeutic effects on precise PTT, which provided potential prospects for future clinical applications. Therefore, this work throws lights on the great potential of BBN@PEG-based nanomedicine for restraining solid tumor and encourages the further exploration of designing an oxygen-vacancy-enhanced PTT model for wide bandgap semiconductor for cancer therapy, which is

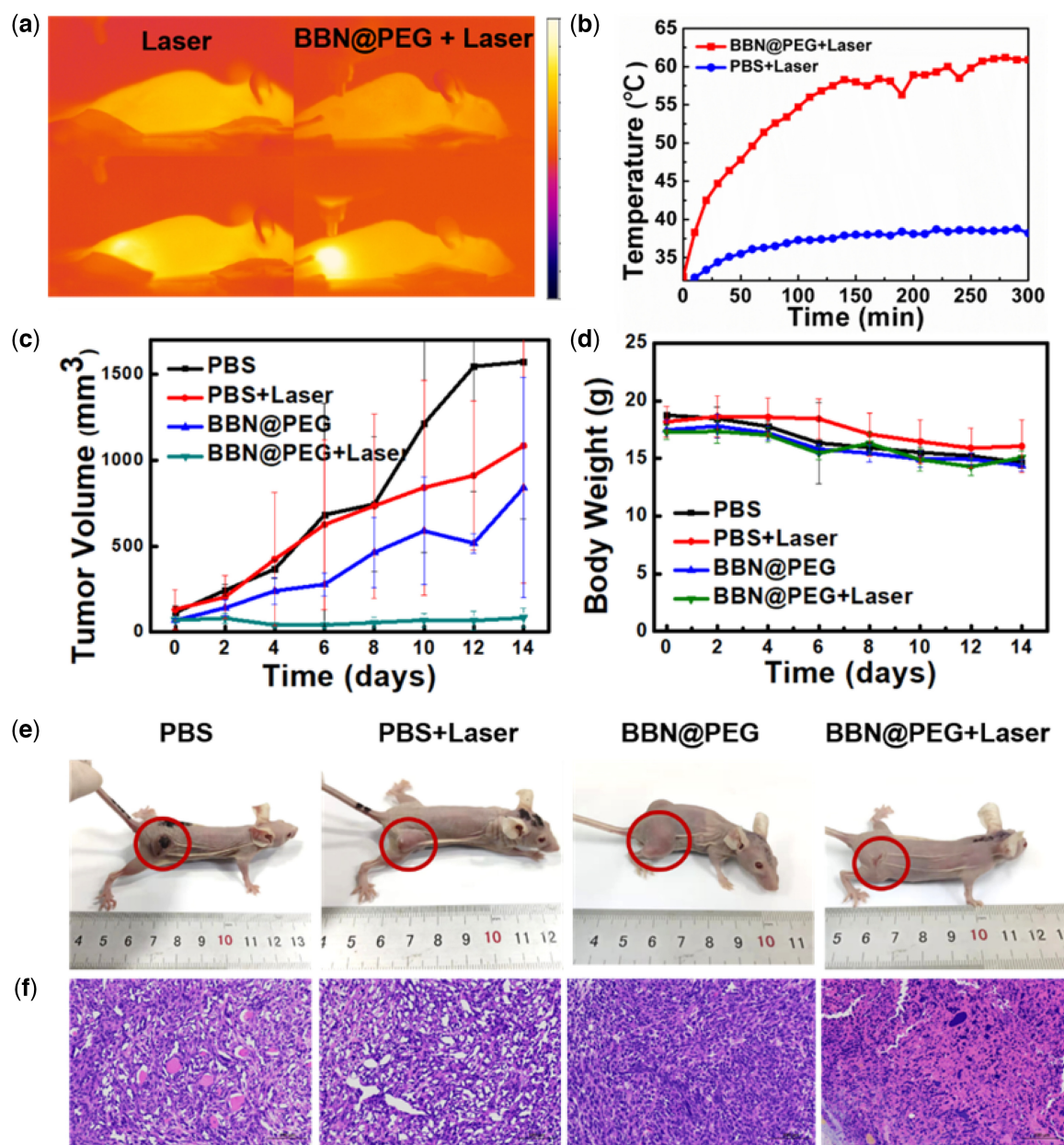


Figure 6. *In vivo* PTT effects of BBN@PEG in 4T1-tumor-bearing mice. (a) *In vivo* thermal imagery and (b) corresponding temperature variation curves of mice *i.v.* injected with PBS, or BBN@PEG NSs (2 mg ml^{-1}) with 808 nm laser irradiation (1 W cm^{-2} , 5 min). (c) Tumor volume curves and (d) body weight change curves of mice intravenously injected with PBS, or BBN@PEG NSs (2 mg ml^{-1}) with or without 808 nm laser irradiation (1 W cm^{-2} , 5 min) (e) the corresponding tumor photographs retrieved on the 16th day. (f) H&E staining sections of tumors of 4 groups dissected.

believed to offer a promising clinical nanoplatform for efficient cancer therapeutics.

Supplementary data

Supplementary data are available at REGGIO online.

Acknowledgements

The authors acknowledge National Synchrotron Radiation Laboratory in Hefei for High End User Cultivation Fund (2020HSC-UE006) and Shanghai Synchrotron Radiation Facility at Line BL15U for X-ray fluorescence imaging.

Funding

This work was supported by the National Natural Science Foundation of China (32025021, 31971292, 51873225), National Key R&D Program of China (2018YFC0910601, 2019YFA0405603), by the Key R&D project of Zhejiang Province (2017C03042, 2020C03110), by the Key Scientific and Technological Special Project of Ningbo City (2017C110022, 2020Z094), by Key Breakthrough Program of Chinese Academy of Sciences (KGZD-EW-T06), by the Natural Science Foundation of Zhejiang province (LY18H180011) and by the Ningbo Natural Science Foundation of China (Grant No. 2014A610158), Ningbo 3315 Innovative Teams Program (2019A-14-C).

Conflicts of interest statement. None declared.

References

- Huang XH, El-Sayed IH, Qian W, El-Sayed MA. Cancer cell imaging and photothermal therapy in the near-infrared region by using gold nanorods. *J Am Chem Soc* **2006**;128:2115–20.
- Liu C, Luo L, Zeng L, Xing J, Xia Y, Sun S, Zhang L, Yu Z, Yao J, Yu Z, Akakuru OU, Saeed M, Wu A. Porous gold nanoshells on functional NH₂-MOFs: facile synthesis and designable platforms for cancer multiple therapy. *Small* **2018**;14:e1801851.
- Boisselier E, Astruc D. Gold nanoparticles in nanomedicine: preparations, imaging, diagnostics, therapies and toxicity. *Chem Soc Rev* **2009**;38:1759–82.
- Jain PK, Huang X, El-Sayed IH, El-Sayed MA. Noble metals on the nanoscale: optical and photothermal properties and some applications in imaging, sensing, biology, and medicine. *Acc Chem Res* **2008**;41:1578–86.
- Liu Y, Bhattarai P, Dai Z, Chen X. Photothermal therapy and photoacoustic imaging via nanotheranostics in fighting cancer. *Chem Soc Rev* **2019**;48:2053–108.
- Yang K, Zhang S, Zhang G, Sun X, Lee S-T, Liu Z. Graphene in mice: ultrahigh in vivo tumor uptake and efficient photothermal therapy. *Nano Lett* **2010**;10:3318–23.
- Wang D, Liu B, Quan Z, Li C, Hou Z, Xing B, Lin J. New advances on the marrying of UCNPs and photothermal agents for imaging-guided diagnosis and the therapy of tumors. *J Mater Chem B* **2017**;5:2209–30.
- Shi Y, Liu M, Deng F, Zeng G, Wan Q, Zhang X, Wei Y. Recent progress and development on polymeric nanomaterials for photothermal therapy: a brief overview. *J Mater Chem B* **2017**;5:194–206.
- Bao Z, Liu X, Liu Y, Liu H, Zhao K. Near-infrared light-responsive inorganic nanomaterials for photothermal therapy. *Asian Journal of Pharmaceutical Sciences* **2016**;11:349–64.
- Ban Q, Bai T, Duan X, Kong J. Noninvasive photothermal cancer therapy nanoplatfoms by integrating nanomaterials and functional polymers. *Biomater Sci* **2017**;5:190–210.
- Zhang Y, Ang CY, Zhao Y. Polymeric nanocarriers incorporating near-infrared absorbing agents for potent photothermal therapy of cancer. *Polym J* **2016**;48:589–603.
- Xia Y, Ma X, Gao J, Chen G, Li Z, Wu X, Yu Z, Xing J, Sun L, Ruan H, Luo L, Xiang L, Dong C, Ren W, Shen Z, Wu A. A flexible caterpillar-like gold nanoparticle assemblies with ultrasmall nanogaps for enhanced dual-modal imaging and photothermal therapy. *Small* **2018**;14:e1800094.
- Sun H, Su J, Meng Q, Yin Q, Chen L, Gu W, Zhang Z, Yu H, Zhang P, Wang S, Li Y. Cancer cell membrane-coated gold nanocages with hyperthermia-triggered drug release and homotypic target inhibit growth and metastasis of breast cancer. *Adv Funct Mater* **2017**;27:1604300.
- Cheng Y, Chang Y, Feng Y, Jian H, Tang Z, Zhang H. Deep-level defect enhanced photothermal performance of bismuth sulfide-gold heterojunction nanorods for photothermal therapy of cancer guided by computed tomography imaging. *Angew Chem Int Ed Engl* **2018**;57:246–51.
- Zhu F, Tan G, Jiang Y, Yu Z, Ren F. Rational design of multi-stimuli-responsive gold nanorod-curcumin conjugates for chemo-photothermal synergistic cancer therapy. *Biomater Sci* **2018**;6:2905–17.
- Yang YJ, Li W. Self-Assembly of gold nanoparticles and multi-walled carbon nanotubes on graphene oxide nanosheets for electrochemical sensing applications. *Fullerenes Nanotubes Carbon Nanostruct* **2018**;26:837–45.
- Zhu F, Tan G, Zhong Y, Jiang Y, Cai L, Yu Z, Liu S, Ren F. Smart nanoplatfom for sequential drug release and enhanced chemo-thermal effect of dual drug loaded gold nanorod vesicles for cancer therapy. *J Nanobiotechnol* **2019**;17(1):44.
- Li W, Han P, Chen Y, Guo Y, Li D, Wu Y, Yue Y, Chu M. Drug-loaded polymer-coated graphitic carbon nanocages for highly efficient in vivo near-infrared laser-induced synergistic therapy through enhancing initial temperature. *ACS Appl Mater Interfaces* **2018**;10:31186–97.
- Chen Y, Guo Y, Han P, Li D, Gui X, Zhang Z, Fu K, Chu M. Graphitic carbon nanocages as new photothermal agent and drug carrier for 980-nm-laser-driven cancer therapy. *Carbon* **2018**;136:234–47.
- Sun S, Zhang L, Jiang K, Wu A, Lin H. Toward high-efficient red emissive carbon dots: facile preparation, unique properties, and applications as multifunctional theranostic agents. *Chem Mater* **2016**;28:8659–68.
- Jia Q, Ge J, Liu W, Zheng X, Chen S, Wen Y, Zhang H, Wang P. A magnetofluorescent carbon dot assembly as an acidic H₂O₂-driven oxygen generator to regulate tumor hypoxia for simultaneous bimodal imaging and enhanced photodynamic therapy. *Adv Mater* **2018**;30:e1706090.
- Wang C, Xu L, Liang C, Xiang J, Peng R, Liu Z. Immunological responses triggered by photothermal therapy with carbon nanotubes in combination with anti-CTLA-4 therapy to inhibit cancer metastasis. *Adv Mater* **2014**;26:8154–62.
- Hassan HA, Smyth L, Wang JT, Costa PM, Ratnasothy K, Diebold SS, Lombardi G, Al-Jamal KT. Dual stimulation of antigen presenting cells using carbon nanotube-based vaccine delivery system for cancer immunotherapy. *Biomaterials* **2016**;104:310–22.
- de Faria PC, dos Santos LI, Coelho JP, Ribeiro HB, Pimenta MA, Ladeira LO, Gomes DA, Furtado CA, Gazzinelli RT. Oxidized multi-walled carbon nanotubes as antigen delivery system to promote superior CD8(+) T cell response and protection against cancer. *Nano Lett* **2014**;14:5458–70.
- Cheng L, Shen S, Shi S, Yi Y, Wang X, Song G, Yang K, Liu G, Barnhart TE, Cai W, Liu Z. FeSe₂-decorated Bi₂Se₃ nanosheets fabricated via cation exchange for chelator-free (64)Cu-labeling and multimodal image-guided photothermal-radiation therapy. *Adv Funct Mater* **2016**;26:2185–97.
- Qumar U, Ikram M, Imran M, Haider A, Ul-Hamid A, Haider J, Riaz KN, Ali S. Synergistic effect of Bi-doped exfoliated MoS₂ nanosheets on their bactericidal and dye degradation potential. *Dalton Trans* **2020**;49:5362–77.
- Chen H, Li Z, Liu X, Zhong J, Lin T, Guo L, Fu F. Colorimetric assay of copper ions based on the inhibition of peroxidase-like activity of MoS₂ nanosheets. *Spectrochim Acta A Mol Biomol Spectrosc* **2017**;185:271–5.
- Han Q, Wang X, Jia X, Cai S, Liang W, Qin Y, Yang R, Wang C. CpG loaded MoS₂ nanosheets as multifunctional agents for photothermal enhanced cancer immunotherapy. *Nanoscale* **2017**;9:5927–34.
- Qian X, Gu Z, Chen Y. Two-dimensional black phosphorus nanosheets for theranostic nanomedicine. *Mater Horiz* **2017**;4:800–16.
- Ren W, Yan Y, Zeng L, Shi Z, Gong A, Schaaf P, Wang D, Zhao J, Zou B, Yu H, Chen G, Brown EMB, Wu A. A near infrared light triggered hydrogenated black TiO₂ for cancer photothermal therapy. *Adv Healthc Mater* **2015**;4:1526–36.
- Ren W, Iqbal MZ, Zeng L, Chen T, Pan Y, Zhao J, Yin H, Zhang L, Zhang J, Li A, Wu A. Black TiO₂ based core-shell

- nanocomposites as doxorubicin carriers for thermal imaging guided synergistic therapy of breast cancer. *Nanoscale* **2017**;9:11195–204.
32. Pan Y, Zhang L, Zeng L, Ren W, Xiao X, Zhang J, Zhang L, Li A, Lu G, Wu A. Gd-based upconversion nanocarriers with yolk-shell structure for dual-modal imaging and enhanced chemotherapy to overcome multidrug resistance in breast cancer. *Nanoscale* **2016**;8:878–88.
33. Wang S, Ren W, Wang J, Jiang Z, Saeed M, Zhang L, Li A, Wu A. Black TiO₂-based nanoprobe for T1-weighted MRI-guided photothermal therapy in CD133 high expressed pancreatic cancer stem-like cells. *Biomater Sci* **2018**;6:2209–18.
34. Jaque D, Martínez Maestro L, del Rosal B, Haro-Gonzalez P, Benayas A, Plaza JL, Martín Rodríguez E, García Solé J. Nanoparticles for photothermal therapies. *Nanoscale* **2014**;6:9494–530.
35. Cheng Y, Zhang H. Novel bismuth-based nanomaterials used for cancer diagnosis and therapy. *Chemistry* **2018**;24:17405–18.
36. Shen PC, Su C, Lin Y, Chou AS, Cheng CC, Park JH, Chiu MH, Lu AY, Tang HL, Tavakoli MM, Pitner G, Ji X, Cai Z, Mao N, Wang J, Tung V, Li J, Bokor J, Zettl A, Wu CI, Palacios T, Li LJ, Kong J. Ultralow contact resistance between semimetal and monolayer semiconductors. *Nature* **2021**;593:211–7.
37. Cheng Y, Kong X, Chang Y, Feng Y, Zheng R, Wu X, Xu K, Gao X, Zhang H. Spatiotemporally synchronous oxygen self-supply and reactive oxygen species production on Z-scheme heterostructures for hypoxic tumor therapy. *Adv Mater* **2020**;32:e1908109.
38. Li H, Li J, Ai Z, Jia F, Zhang L. Oxygen vacancy-mediated photocatalysis of BiOCl: reactivity, selectivity, and perspectives. *Angew Chem Int Ed Engl* **2018**;57:122–38.
39. Singh S, Sharma R, Khanuja M. A review and recent developments on strategies to improve the photocatalytic elimination of organic dye pollutants by BiOX (X=Cl, Br, I, F) nanostructures. *Korean J Chem Eng* **2018**;35:1955–68.
40. Guo Z, Zhu S, Yong Y, Zhang X, Dong X, Du J, Xie J, Wang Q, Gu Z, Zhao Y. Synthesis of BSA-Coated BiOI@Bi₂S₃ semiconductor heterojunction nanoparticles and their applications for radio/photodynamic/photothermal synergistic therapy of tumor. *Adv Mater* **2017**;29(44):1704136.
41. Xu Y, Shi Z, Zhang L, Brown EM, Wu A. Layered bismuth oxyhalide nanomaterials for highly efficient tumor photodynamic therapy. *Nanoscale* **2016**;8:12715–22.
42. Dai C, Hu R, Wang C, Liu Z, Zhang S, Yu L, Chen Y, Zhang B. Defect engineering of 2D BiOCl nanosheets for photonic tumor ablation. *Nanoscale Horiz* **2020**;5:857–68.